Manuscript version: Author's Accepted Manuscript
The version presented in WRAP is the author's accepted manuscript and may differ from the published version or Version of Record.

Persistent WRAP URL:
http://wrap.warwick.ac.uk/114452

How to cite:
Please refer to published version for the most recent bibliographic citation information.
If a published version is known of, the repository item page linked to above, will contain details on accessing it.

Copyright and reuse:
The Warwick Research Archive Portal (WRAP) makes this work by researchers of the University of Warwick available open access under the following conditions.

Copyright © and all moral rights to the version of the paper presented here belong to the individual author(s) and/or other copyright owners. To the extent reasonable and practicable the material made available in WRAP has been checked for eligibility before being made available.

Copies of full items can be used for personal research or study, educational, or not-for-profit purposes without prior permission or charge. Provided that the authors, title and full bibliographic details are credited, a hyperlink and/or URL is given for the original metadata page and the content is not changed in any way.

Publisher's statement:
Please refer to the repository item page, publisher's statement section, for further information.

For more information, please contact the WRAP Team at: wrap@warwick.ac.uk.

Improved on-the-fly MCTDH simulations with many-body-potential tensor decomposition and projection diabatisation

Gareth W. Richings, Christopher Robertson, and Scott Habershon[*]

Department of Chemistry and Centre for Scientific Computing, University of Warwick, Coventry, CV4 7AL, UK

E-mail: s.habershon@warwick.ac.uk

Abstract

We have recently demonstrated how potential energy surface (PES) interpolation methods such as kernel ridge regression (KRR), can be combined with accurate wavefunction time-propagation methods, specifically the multi-configuration time-dependent Hartree (MCTDH) method, to generate a new "on-the-fly" MCTDH scheme (DD-MCTDH) which does not require the pre-fitting of the PES which is normally required by MCTDH. Specifically, we have shown how our DD-MCTDH strategy can be used to model non-adiabatic dynamics in a 4-mode/2-state model of pyrazine, with *ab initio* electronic structure calculations performed directly during propagation, requiring around 100 hours of computer wall-time. In this Article, we show how the efficiency and accuracy of DD-MCTDH can be dramatically improved further still by: (i) using systematic tensor decompositions of the KRR PES, and (ii) using a novel scheme for diabatisation within the framework of configuration interaction (CI) methods which only requires local adiabatic electronic states, rather than non-adiabatic coupling matrix elements. The result of these improvements is that our latest version of DD-MCTDH can perform a 12-mode/2-state simulation of pyrazine, with PES evaluations at CAS level, in just 29-90 hours on a standard desktop computer; this work therefore represents an enormous step towards direct quantum dynamics with MCTDH.

1 Introduction

Over the last three decades, the multi-configuration time-dependent Hartree (MCTDH) method has found widespread application in modelling both ground-state and excited-state chemical processes in complex molecular systems.[1–6] In MCTDH, the time-dependent Schrödinger equation (TDSE) is solved by introducing a wavefunction *ansatz* comprising a sum of Hartree products of single-particle functions (SPFs), along with their complex expansion coefficients; using the Dirac-Frenkel time-dependent variational principle,[7–9] one can then derive equations-of-motion for both the expansion coefficients *and* the SPFs, leading to an efficient method for propagating wavepackets which can, in principle, be converged to the exact quantum-mechanical result. The range of systems modelled to date with MCTDH is continually growing, spanning non-adiabatic dynamics in organic molecules,[2,10,11] transport on model surfaces,[12–14] and organometallic complexes.[15,16]

In practice, two important general factors have constrained the application domain of MCTDH simulations. First, although ameliorated by adoption of a basis of time-dependent SPFs, MCTDH exhibits poor scaling with system size;[6,17] in general, systems with a few tens of active degrees-of-freedom represent the current upper limit for the standard MCTDH methodology. However, recent development of multi-layer MCTDH (ML-MCTDH[18–20]) has significantly pushed back this limit; recent work has demonstrated how ML-MCTDH can simulate quantum dynamics on model potential energy surfaces (PESs) described by $\sim 10^3$ degrees-of-freedom, with a representative application of ML-MCTDH being the modelling of electron injection from an organic dye molecule (coumarin) into the surface of TiO_2 using a parameterized model comprising ~ 50 vibrational normal-mode coordinates and a quasi-continuum of acceptor electronic states.[21]

The second pressing problem in employing MCTDH to study quantum dynamics in general molecular systems relates to the PES itself. In common with all methods based on propagation of a wavefunction described as a linear combination of basis functions, MCTDH time-propagation requires evaluation of PES matrix elements as integrals over the entire

coordinate space; as a result, one technically requires a *global* PES representation from the outset of the calculation. In many wavefunction propagation methods, notably those based on Gaussian wavepacket (GWP) basis functions,[22–41] the localized nature of the basis functions themselves can be exploited to evaluate PES matrix elements by introducing local approximations such as Taylor expansions.[29,42] However, the SPFs typically employed in MCTDH are semi-local in nature, and time-evolve to optimally conform to the TDSE; as a result, application of local approximations of PES matrix elements is usually insufficiently accurate. In addition, the Hartree product wavefunction *ansatz* employed in MCTDH puts constraints on the functional form of any global PES; in particular, the PES must be available as a sum-of-products function to enable efficient MCTDH propagation.[6,17]

The standard approach to address the important "PES problem" in MCTDH is to attempt to cast the global PES of the system into a sum-of-products form using a fitting procedure. For example, a common approach when studying non-adiabatic dynamics is to fit a (quadratic) vibronic coupling Hamiltonian;[12,15,43,44] this approach has been successfully to model non-adiabatic dynamics in several molecular systems, but clearly introduces significant assumptions about the form of the PES and the role of coupling between different electronic and nuclear degrees-of-freedom. Similarly, the POTFIT methodology[45,46] has emerged as a standard route towards fitting sum-of-product PESs for MCTDH, and has again been widely applied to a number of complex molecular systems, although the fundamental incompatibility between POTFIT-like methods and local *ab initio* electronic structure remains.

Attempts to move MCTDH away from the requisite sum-of-products PES include the correlation DVR approach,[47] although the challenge of applying this methodology to combined SPFs in MCTDH persists. More recently, the collocation MCTDH method of Carrington was proposed to simplify MCTDH propagation and PES matrix evaluation by using a collocation method which only requires PES values at a smaller number of grid-points than the full-grid required to define the wavefunction.[48] This strategy has been successfully used

to study the vibrational eigenstates of CH_3 by imaginary-time propagation; application to real-time quantum dynamics would further demonstrate the utility of this strategy.

Our own recent work in this area,[49–51] and the focus of this Article, has demonstrated how MCTDH wavefunction propagation can be combined with machine-learning strategies for interpolation in order to auto-generate PESs in tandem with wavefunction time-evolution. In our approach, we employ Kernel Ridge Regression (KRR) to generate a semi-global PES describing the vicinity of the evolving wavefunction using just a few PES evaluations at selected reference geometries; because the PES is generated during the wavefunction propagation itself, no pre-fitting of the PES is required. We have already shown that our direct-dynamics MCTDH (DD-MCTDH) strategy can be used to model non-adiabatic dynamics of molecules such as pyrazine and salicylaldimine by directly calling *ab initio* electronic structure calculations when necessary. As a representative example, we have shown that a MCTDH propagation of a 4-mode/2-electronic-state model of pyrazine, with PES evaluations performed at CAS(8,8) level, can be performed in around 100 hours on a single desktop CPU; no PES fitting is required.

Despite the development of DD-MCTDH approach over the last year or so, significant computational hurdles remain; the aim of this paper is to show how these can be addressed. In particular, we note that: (i) our current PES auto-generation scheme can only couple *pairs* of degrees-of-freedom, leading to inaccuracies due to neglect of higher-order mode-couplings, (ii) the scheme we have employed previously for transforming adiabatic electron states into diabatic states required the non-adiabatic coupling matrix elements,[33] which can be expensive to evaluate, and (iii) the stochastic nature of our current approach to selecting reference configurations for KRR PES generation leads to some 'jitter' in expectation values calculated between different simulations of the same system.

Here, we systematically introduce and assess new computational strategies to address each of these challenges. As shown below, the upshot of these developments is that we can now perform a *12-mode/2-electronic-state* simulation of pyrazine (*i.e.* three times larger

4

than our previous simulation noted above) in 29-90 hours on a single desktop computer, depending on the requisite accuracy of the PES. As a result, this Article makes significant steps towards making accurate wavefunction propagation methods like MCTDH available as general-purpose tools for interrogating molecular quantum dynamics.

2   Methodology

In this Section, we review the standard grid-based quantum dynamics methodology and our existing DD-MCTDH strategy. In Sections 3-6, we then systematically highlight four computational improvements of DD-MCTDH to improve both efficiency and accuracy; these include using Cholesky decomposition to accelerate KRR PES variance evaluation, improving simulation reproducibility by using Sobol sequence sampling, improving KRR PES accuracy using tensor decomposition, and efficiently generating diabatic PESs using a recently-developed diabatisation scheme based on the projection of configuration interaction (CI) coefficients. Finally, in Section 7, we highlight the result of these method developments by performing *ab initio* DD-MCTDH propagation of a 12-mode/2-state model of pyrazine.

2.1   Grid-Based Quantum Dynamics: The Standard Method

For the following discussion, it is useful to describe the standard grid-based method for quantum dynamics.[17] For a molecular system with f degrees-of-freedom, the wavefunction is expanded as a sum-of-products of time-independent basis functions (which are usually point-like discrete variable representation (DVR) functions), each of which has an associated, time-dependent, complex coefficient, $C_{j_1,\cdots,j_f}$. For a nuclear wavepacket moving on electronic

state, s, we then have

$$
\begin{aligned}
\Psi^{(s)}(q_1, \cdots, q_f, t) &= \sum_{j_1=1}^{N_1} \cdots \sum_{j_f=1}^{N_f} C_{j_1, \cdots, j_f}^{(s)}(t) \prod_{\kappa=1}^{f} \chi_{j_\kappa}^{(\kappa)}(q_\kappa) \\
&= \sum_{J} C_J^{(s)}(t) X_J(\mathbf{q}),
\end{aligned}
\tag{1}
$$

where we have introduced a compound index, $J = j_1, \cdots, j_f$. The basis function $\chi_{j_\kappa}^{(\kappa)}(q_\kappa)$ indicates the j_κ-th one-dimensional function along degree-of-freedom κ, with q_κ indicating the corresponding coordinate.

If there are N_s orthonormal electronic states, labelled $|i\rangle$, the total wavefunction can be written as

$$
|\Psi\rangle = \sum_{s=1}^{N_s} |\Psi^{(s)}\rangle |s\rangle.
\tag{2}
$$

Writing the total Hamiltonian as a general sum over electronic state Hamiltonian elements $\hat{H}^{(su)}$ evaluated for electronic states $|s\rangle$ and $|u\rangle$, we have,

$$
\hat{H} = \sum_{su}^{N_s} |s\rangle \hat{H}^{(su)} \langle u|,
\tag{3}
$$

and employing the Dirac-Frenkel variational principle,[7,8] yields set of coupled equations-of-motion for the expansion coefficients,

$$
i\hbar \dot{C}_J^{(s)} = \sum_{u=1}^{N_s} \sum_{L} \langle X_J | \hat{H}^{(su)} | X_L \rangle C_L^{(u)}.
\tag{4}
$$

These equations-of-motion can be integrated to propagate the wavefunction in time; with a sufficiently large product basis, this approach provides a numerically exact solution of the TDSE. This method is referred to as the standard method (SM)[17] hereafter.

6

2.2 Grid-Based Quantum Dynamics: MCTDH

Practical applications of the SM are limited to about 5 degrees-of-freedom; to enable simulations of larger molecular systems, MCTDH was developed. In common with the SM, the MCTDH wavefunction is expanded in a sum-of-products of basis functions, with each product having an independent expansion coefficient, $A_{j_1,\cdots,j_m}^{(s)}(t)$. So, we have

$$
\begin{aligned}
\Psi^{(s)}(Q_1,&\cdots,Q_f,t)\\
&= \sum_{j_1=1}^{n_1}\cdots\sum_{j_m=1}^{n_m} A_{j_1,\cdots,j_m}^{(s)}(t)\prod_{\kappa=1}^{m}\varphi_{j_\kappa}^{(s,\kappa)}(Q_\kappa,t)\\
&= \sum_J A_J^{(s)}(t)\,\Phi_J^{(s)}(\mathbf{Q},t),
\end{aligned}
\tag{5}
$$

where $\varphi_{j_\kappa}^{(s,\kappa)}(Q_\kappa,t)$ is the j_κ-th basis function on electronic state s and Q_κ indicates the corresponding degree(s)-of-freedom.

Unlike the SM, the basis functions in MCTDH are *time-dependent*; employing the MCTDH *ansatz* and Dirac-Frenkel variational principle yields equations-of-motion for both coefficients and time-dependent basis functions (referred to as single-particle functions [SPFs]):

$$
i\hbar\dot{A}_J^{(s)} = \sum_{u=1}^{N_s}\sum_L \langle\Phi_J^{(s)}|\hat{H}^{(su)}|\Phi_L^{(u)}\rangle A_L^{(u)},
\tag{6a}
$$

$$
i\hbar\dot{\boldsymbol{\varphi}}^{(s,\kappa)} = \left(1-\hat{P}^{(s,\kappa)}\right)\left(\boldsymbol{\rho}^{(s,\kappa)}\right)^{-1}\sum_{u=1}^{N_s}\langle\hat{H}^{(su)}\rangle^{(\kappa)}\boldsymbol{\varphi}^{(u,\kappa)}.
\tag{6b}
$$

Here, $\hat{P}^{(s,\kappa)}$ is a projection operator onto the SPF space along mode κ, and $\left(\boldsymbol{\rho}^{(s,\kappa)}\right)^{-1}$ is the inverse of the density matrix associated with κ. By constructing a Hartree product of SPFs in all modes apart from κ, $\Phi_{J^\kappa}^{(s)}$, we can define a set of single-hole functions, $\Psi_l^{(s,\kappa)} = \sum_{J^\kappa} A_{J_l^\kappa}^{(s)}\Phi_{J^\kappa}^{(s)}$, from which a mean-field matrix, with elements $\langle\hat{H}^{(su)}\rangle_{jl}^{(\kappa)}=\langle\Psi_j^{(s,\kappa)}|\hat{H}^{(su)}|\Psi_l^{(u,\kappa)}\rangle$, is defined.

Most commonly, the SPFs, $\boldsymbol{\varphi}^{(s,\kappa)}$, are assumed to be functions of a small subset (usually

1-4) of the degrees-of-freedom in the system, $Q_\kappa = (q_{\kappa_1}, \cdots, q_{\kappa_p})$. The SPFs themselves are expanded in terms of an underlying time-independent basis set,

$$\varphi_{j_\kappa}^{(s,\kappa)}(Q_\kappa, t) = \sum_{i_\kappa=1}^{N_\kappa} c_{i_\kappa}^{(s,\kappa,j_\kappa)}(t) X_{i_\kappa}^{(\kappa)}(Q_\kappa), \tag{7}$$

with $X_{i_\kappa}^{(\kappa)}(Q_\kappa)$ identifying the i_κ-th basis function for coordinate Q_κ. By evolving the SPFs variationally, the number required for accurate wavefunction representation can be kept to a minimum. This reduction in total basis set size enables MCTDH to study larger molecular systems than the SM (noting that MCTDH also scales exponentially, but with a smaller base than the SM[17]).

2.3 Direct Dynamics Using Kernel Ridge Regression

Previously, we have shown how one can construct a direct-dynamics grid-based (DD-GB) scheme for wavefunction propagation based on either the SM or MCTDH.[49–51] Here a representation of the global PES is constructed on-the-fly using KRR interpolation.[52] Defining a one-dimensional kernel along degree-of-freedom λ, centered at q_λ^l with a width defined by the free (positive) parameter α, as

$$k(q_\lambda, q_\lambda^l) = e^{-\alpha(q_\lambda - q_\lambda^l)^2}, \tag{8}$$

we can build a general kernel in f system dimensions as

$$\begin{aligned}
k^{\mathrm{f}}(\mathbf{q}, \mathbf{q}^l) = \sum_{\lambda=1}^{f} k(q_\lambda, q_\lambda^l) + \sum_{\lambda,\mu}^{f} k(q_\lambda, q_\lambda^l) k(q_\mu, q_\mu^l) \\
+ \cdots + \prod_{\lambda=1}^{f} k(q_\lambda, q_\lambda^l).
\end{aligned} \tag{9}$$

That is, the general kernel can be written as sum of Gaussian functions of increasing dimensionality, centered at the molecular geometry represented by coordinate $\mathbf{q}^l = (q_1^l, \cdots, q_f^l)$.

To represent the full PES operator, a linear combination of kernel functions, centered at a selection of M molecular geometries (or reference points), $\{\mathbf{q}^l\}$, is formed

$$V^{\text{KRR}}_{(su)}(\mathbf{q}) \approx \sum_{l=1}^{M} w_l^{(su)} k(\mathbf{q}, \mathbf{q}^l). \tag{10}$$

Here, $w_l^{(su)}$ is the weight of the l-th kernel function in the diabatic PES term for electronic states s and u.

It should be clear from Eqs. (9) and (10) that the PES operator has the sum-of-products form necessary for efficient propagation of the equations-of-motion of the SM and MCTDH methods. Note that we have dropped the superscript from the kernel in Eq. 10; this is because the general kernel in Eq. (9) is not used in practice (except for low-dimensional examples). Instead, in our previous work, we have used truncated versions of the general kernel; the initial implementation of our approach[49,51] restricted the kernel to the final, f-dimensional term *i.e.* $k(\mathbf{q}, \mathbf{q}^l) = \prod_{\lambda=1}^{f} k(q_\lambda, q_\lambda^l)$ (termed the full kernel), whilst in our most recent work we introduced the so-called additive kernel up to second-order (*i.e.* where only the first two terms of Eq. (9) are retained[50]). Both truncations are valid within the theory of KRR, being both symmetric and positive semi-definite.

The coefficients in Eq. (10), $\{w_l^{(su)}\}$, are determined by solving the set of linear equations

$$\mathbf{Kw} = \mathbf{b}, \tag{11}$$

where $\mathbf{w}$ is the vector of desired coefficients and $\mathbf{b}$ is a vector holding the actual values of the (diabatic) potential energy calculated at the molecular geometries $\{\mathbf{q}^l\}$,

$$b_l = V^{(su)}\left(\mathbf{q}^l\right). \tag{12}$$

The covariance matrix, $\mathbf{K}$, has elements

$$K_{mn} = k(\mathbf{q}^m, \mathbf{q}^n) + \gamma^2 \delta_{mn}. \tag{13}$$

where γ^2 is a small, positive number acting as a regularisation parameter.

In addition to the compact representation of the PES given in Eq. (10), KRR provides a useful estimate to the quality of fit of the KRR PES through the definition of a variance function,[52]

$$\sigma^2(\mathbf{q}) = k(\mathbf{q}, \mathbf{q}) + \gamma^2 - \mathbf{k}^{\mathrm{T}} \mathbf{K}^{-1} \mathbf{k}, \tag{14}$$

where the vector $\mathbf{k}$ holds values of the kernel evaluated at the test point $\mathbf{q}$, such that $k_i = k(\mathbf{q}, \mathbf{q}^i)$.

We have implemented on-the-fly generation of a KRR PES, combined with the SM and MCTDH methods of quantum dynamics,[49–51] in a development version of the Quantics package.[53] Upon initialization of wavepacket propagation, we first generate an approximation to the PES using KRR: this is achieved by sampling a number of molecular geometries around the current wavepacket center, and then evaluating the electronic energies (using, for example, either a parameterised PES or *ab initio* electronic structure calculation) at the selected geometries. These energies and geometries are stored in a database. After sampling and energy evaluations, Eq. (11) is solved to give the weights in Eq. (10) to form the PES operator, and wavepacket propagation proceeds. After wavepacket propagation for a short, fixed amount of time (typically a femtosecond), further sampling of configuration space is performed, with new geometries accepted or rejected based on the current KRR variance estimate given by Eq. 14. The new energies and geometries are combined with those in the existing database, a new approximation to the KRR PES is generated, and wavepacket propagation continues. This propagate-sample-propagate scheme is repeated until the end of the dynamics calculations, with the database of energies constantly adapting to give an accurate representation of the true PES.

3 Cholesky Update for Efficient Variance Estimation

We begin by describing a straightforward adaptation of the above algorithm which has an important impact on propagation simulation times. In our original on-the-fly KRR PES generation scheme, new molecular geometries are sampled randomly within a pre-determined range of the center of the wavepacket and the KRR variance (Eq. (14)) at each geometry is evaluated. If the variance is below a user-defined tolerance parameter, the KRR representation of the PES at that geometry is assumed to be sufficiently accurate, and no further energy evaluations are performed. If the KRR variance is above the tolerance, a new energy evaluation is performed and the result is added to the database. We have found that direct inversion of the covariance matrix, $\mathbf{K}$, (Eq. 11) becomes prohibitively expensive as the PES database grows, ultimately becoming a major contribution to overall calculation time.[49–51] In addition, because we choose to only invert the covariance matrix once at the start of each sampling step, the calculated variances do not account for any geometries which are newly-added to the PES database until the *next* sampling step; as a result, there is a danger of unnecessarily over-sampling in some regions of configuration space.

To improve this situation, three features of $\mathbf{K}$ can be exploited: (i) it is symmetric, positive definite, (ii) it grows as more sample points are added to the database of energies, and (iii) each new point added to the database simply adds a new row and column to $\mathbf{K}$, without affecting any of the exising elements K_{mn}. The symmetric, positive definite nature of $\mathbf{K}$ means that one can perform a Cholesky decomposition,

$$\mathbf{K} = \mathbf{L}\mathbf{L}^T \tag{15}$$

where $\mathbf{L}$ is a lower triangular matrix, in order to solve Eq. (11) and to evaluate Eq. (14). Additionally, because the majority of the covariance matrix does not change when new database points are added, there is no need to repeatedly carry out a full decomposition before each sampling step; instead, a more efficient matrix update can be performed when

new points are added. The well-known procedure for updating a Cholesky decomposition of the matrix $\mathbf{K}$ when new rows and columns are added to the original matrix[54] is given in the *Supporting Information* for completeness, but the upshot of this update approach is that one no longer needs to invert the full $\mathbf{K}$ matrix to determine the new KRR weights whenever new points are added. As a result, evaluation of the variance at any tested reference geometry is faster. The Cholesky update is performed after every new geometry is added to the database, meaning that the variance for the next sampled geometry is based on all points in the database, not just those sampled in previous steps.

To illustrate the effect of this algorithm update, we investigate the dynamics of proton transfer in salicylaldimine, as studied in our previous work.[50] Here, we calculate wavepacket flux across the PES barrier along the proton stretching mode (labelled v_1), using a six-member subset of the mass-frequency scaled normal modes centered at the transition state. Full details of the propagation conditions are given in Section IV.C in Ref. 50 and are not repeated here; the same calculation was performed here, but this time using the Cholesky update procedure. Results of the two calculations (with and without Cholesky update) are shown in Fig. 1(a); clearly, there is very little difference between the two results shown, especially when one considers the sensitivity of wavepacket flux to propagation conditions. We conclude that the modified algorithm has not impacted on the accuracy of propagation. However, there is a clear difference in the calculation times (both carried with the same single-CPU desktop computer). Table 1 shows total CPU times for both calculations, along with timings for the solving the equations-of-motion and the equations used in KRR fitting of the PES. In addition, Fig. 1(b) provides a graphical representation of the huge saving in total CPU time when switching to the Cholesky update algorithm (89% overall), and Fig. 1(c) shows the percentage of the times of the respective calculations taken up with evaluating Eq. (14). Using the old algorithm, nearly 90% of the total CPU time was used to calculate the KRR variance; Cholesky update reduces this to just 3.2%.
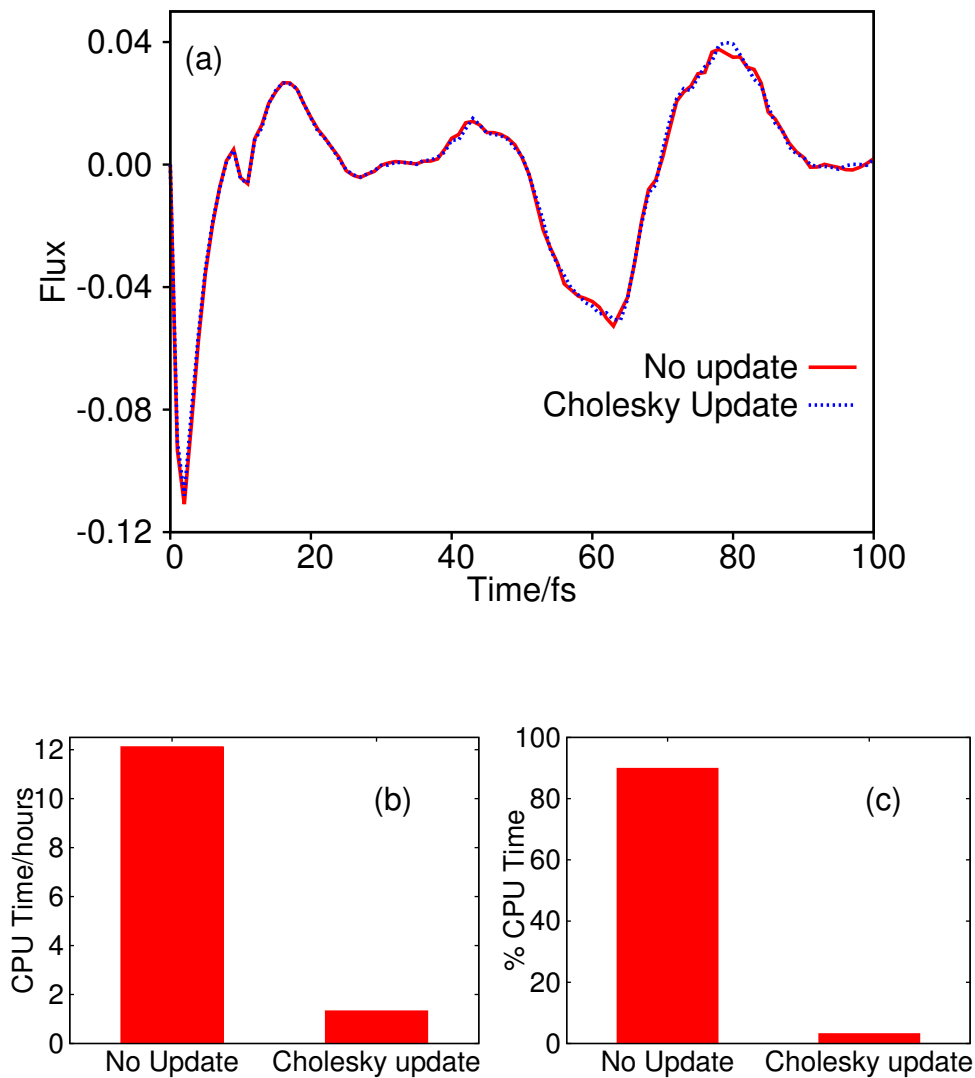
Figure 1: Effect of Cholesky update for solution of Eqs. (11) and (14). (a) Wavefunction flux in the proton transfer of a six-mode model of salicylaldimine with (red, solid line) and without (blue, dashed line) Cholesky update. (b) Total CPU time (in hours) to run wavepacket propagations from (a) using a single processor on a desktop machine with and without Cholesky update. (c) Percentage of total CPU time spent evaluating Eq. (14) with and without Cholesky update.

Table 1: Summary of performance improvement gained by implementing Cholesky update when solving Eqs. (11) and (14) in a six-mode simulation of salicylaldimine. (a) Time needed to solve the MCTDH equations-of-motion. (b) Time needed to solve Eq. (11). (c) Time needed to evaluate Eq. (14).

	Without Cholesky update	**With** Cholesky update
Total CPU/s	43,628	4,796
Integrator[a] CPU/s	3,807	3,974
Variance[b] CPU/s	39,201	154
KRR Weights[c] CPU/s	82	0.3
Database Entries	2,185	2,081
PES Operator Terms	134	137

We also see from Table 1 that the number of configurations added to the database is somewhat reduced when using Cholesky update, although the number of terms in the final PES operator (after singular value decomposition; see Ref. 50) is broadly similar. The change in the number of database entries is a consequence of the improved variance estimation using Cholesky update, while the small change in the number of potential terms (allied with random sampling used to select the molecular geometries for the sample set) explains the slight differences in the wavepacket flux seen in Fig. 1(a).

We conclude that the implementation of the well-known Cholesky update algorithm to solve Eqs. (11) and (14) provides an enormous saving in computation time when compared to the original method, and consequently means that calculations on much larger systems become feasible within a reasonable time; all results reported subsequently here use the Cholesky update approach.

4   Sobol sequence sampling of configuration space

The second algorithmic update implemented here is sampling of configuration space using Sobol sequences[55] when selecting molecular geometries to construct the KRR PES. Our earlier implementation, employed in Section 3, relies on *random* selection of geometries from a uniform distribution centered on the evolving wavepacket. The randomly-generated

geometries are rejected or accepted for energy evaluation based on the calculated KRR variance. This stochastic method for sampling configurations leads to non-repeatability in the dynamics calculations; this obviously conflicts with the deterministic nature of the TDSE.

To circumvent the 'jitter' caused by different PES samplings, we have implemented an algorithm to select geometries based upon Sobol sampling. The merits of this sampling method are its deterministic nature and its uniformity (*i.e.* all regions of space are sampled if enough points are selected). In addition, Sobol sampling enables one to systematically increase the fineness of the sample as more points are added.

The Sobol sequence algorithm generates a set of points, $\mathbf{x}_1 \cdots , \mathbf{x}_N$, in the f-dimensional unit cube, $I^f = [0,1]^f$. Importantly, the Sobol sequence generates configurations in a reproducible sequence, yet in such as way that the discrepancy with previous configurations is low. In employing Sobol sequences to sample configurations in order to generate a KRR PES, the procedure is very similar to that used with a random number generator:

1. As required during wavepacket propagation, the region of configuration space to be sampled is defined as the f-dimensional cube centered on the position expectation value of the wavepacket and extending by a multiple of the wavepacket width in both directions along the respective dimensions.

2. The Sobol sequence is initialised by generating direction numbers as described in the *Supplementary Information*.

3. The first member of the Sobol sequence is generated using the Sobol sequence recurrence relation for for each dimension.

4. The Sobol number for the j-th dimension is rescaled by the total length of the sample region along the dimension, then shifted to lie within the targeted region of configuration space; this is repeated for all dimensions.

5. At the resulting geometry Eq. (14) is evaluated and, if the variance is smaller than the

user-supplied threshold, the point is rejected. Otherwise the potential energy value is evaluated (for example, using *ab initio* electronic structure methods) and stored.

6. Repeat steps 3-5 to generate a pre-defined number of configurations, then generate the new KRR PES and continue with wavefunction propagation.

To test the impact of Sobol sampling, we study the same six-mode salicylaldimine model as studied in Section 3. In Fig. 2, we show the wavepacket flux across the proton transfer potential barrier, and compare simulations performed using a randomly-sampled set of points in the KRR PES to another simulation which builds the KRR PES using geometries selected by the Sobol sequence procedure outline above. Clearly the agreement between the plots is excellent; Sobol sampling does not change the accuracy of the resulting PES, but has the added advantage of simple reproducibility. In addition, we find that 2081 database entries (molecular configurations) were created using the random method whilst only 1882 were produced by the Sobol sequences, a decrease of around 10%. The difference here emerges as a result of the different space-spanning properties of the sampled configurations, with the Sobol sequence implicitly generated to fill in voids in configuration space.

To conclude, Sobol sequence sampling of the KRR PES geometries is as accurate as random sampling, but with the additional possibility of fewer energy evaluations. However, the main benefit of the Sobol sampling method is its repeatability; identical results are obtained when using the same initial conditions, something which cannot be said for the random sampling method. All subsequent results reported here have used the Sobol algorithm.

5   Tensor decomposition of a KRR PES

Previously,[50] we set out the difficulties in running MCTDH dynamics using a KRR PES employing a full-dimensional kernel; in particular, the resulting large number of terms in the PES expansion (Eq. (10)) causes the solution of the equations-of-motion to become very computationally-demanding. The solution offered in our previous work was to perform a
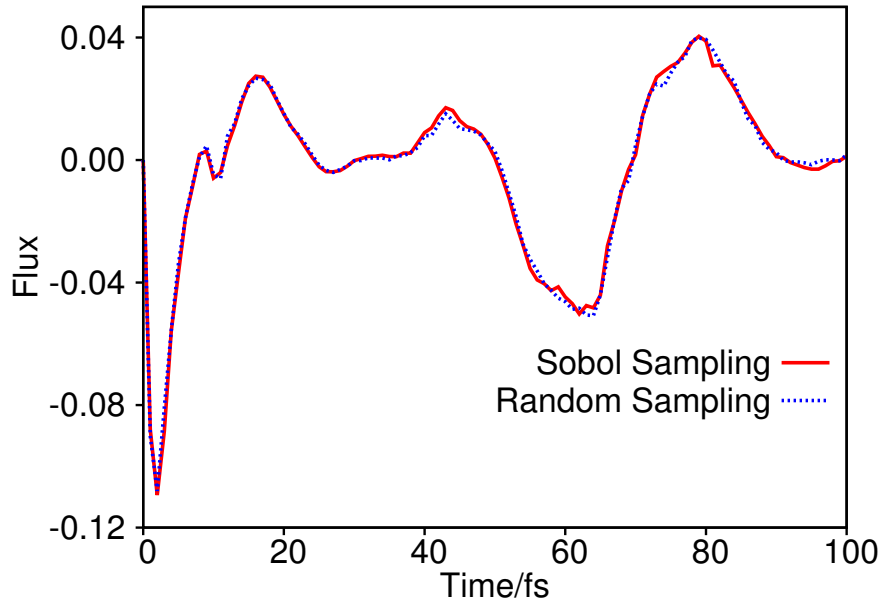
Figure 2: Wavefunction flux expectation values for proton transfer in salicylaldimine. The red, solid line shows the flux calculated with the PES generated by sampling configuration space using Sobol sequences. The blue, dashed line shows the flux calculated using random sampling of configuration space.

secondary fitting to the KRR PES in order to significantly reduce the number of terms in the PES operator and reduce the effort required to propagate the equations-of-motion. Specifically, we noted that the functional form of the terms in the PES operator is of no importance when using grid-based dynamics methods because the matrix elements in the DVR basis are simply given by the value of the PES terms at the location of each grid-point. Exploiting this fact, we proposed the following fitting scheme:

1. Evaluate $V^{\text{KRR}}(\mathbf{0})$ at the coordinate origin.

2. Evaluate V^{KRR} at all gridpoints along each degree-of-freedom (subtracting $V^{\text{KRR}}(\mathbf{0})$ along all bar one); we therefore have the one-dimensional operator terms as a set of f vectors.

3. For each pair of degrees-of-freedom, λ and μ, construct a two-dimensional grid from the coordinates of the DVR gridpoints along each, (q_λ^l, q_μ^m), and evaluate V^{KRR} at each point (setting all other coordinates to 0). At each point, evaluate the residual by

17

subtracting the relevant one-dimensional terms from the KRR potential

$$V^{\lambda\mu}(q_\lambda^l, q_\mu^m) = V^{\mathrm{KRR}}(q_\lambda^l, q_\mu^m) - V^\lambda(q_\lambda^l) - V^\mu(q_\mu^m) - V^{\mathrm{KRR}}(\mathbf{0}), \tag{16}$$

to give a $N_\lambda \times N_\mu$ matrix.

4. For use in an MCTDH calculation the residual must be decomposed into the product of terms along each individual degree-of-freedom. To do so, we perform a singular value decomposition (SVD) on the residual matrix such that

$$V^{\lambda\mu}(q_\lambda^l, q_\mu^m) = \sum_{j=1}^{\min(N_\lambda, N_\mu)} \sigma_j\, u_{lj}\, w_{mj} \tag{17}$$

Setting

$$V_{\lambda(j)}^{\lambda\mu}(q_\lambda^l) = \sqrt{\sigma_j} u_{lj} \tag{18a}$$

$$V_{\mu(j)}^{\lambda\mu}(q_\mu^m) = \sqrt{\sigma_j} w_{mj} \tag{18b}$$

we have that

$$\mathbf{V}^{\lambda\mu} = \sum_{j=1}^{\min(N_\lambda, N_\mu)} \mathbf{V}_{\lambda(j)}^{\lambda\mu} \otimes \mathbf{V}_{\mu(j)}^{\lambda\mu} \tag{19}$$

giving a sum of outer products of vectors as required by MCTDH.

5. To reduce computational effort further still, it is desirable to leave out terms which contribute little to the accuracy of the PES. It can be shown that, by including only the first n terms in the sum in Eq. (19), the squared Frobenius norm of the residual is

$$||\mathbf{R}|| = \sum_{j=n+1}^{\min(N_\lambda, N_\mu)} \sigma_j^2. \tag{20}$$

The terms with the largest singular values are included in the final potential expansion, such that $||R||$ falls below some user-defined threshold.

6. Repeat for all pairs of degrees-of-freedom.

As noted above, this procedure was used in the salicylaldimine calculations presented in Section 3 with the threshold for $||R||$ set to 10^{-3}.

This fitting procedure is based on the idea that the major contributions to the accurate representation of the true PES are those low-dimensional terms which couple a small number of degrees-of-freedom; this is essentially the same ethos behind the high-dimensional model representation of the PES.[56–58] As such, including terms up to second-order (*i.e.* those which couple wavepacket motion in two degrees-of-freedom) is expected to give a good representation of the PES in many cases. However, there will be cases where it is necessary to go beyond coupled pairs of degrees-of-freedom in order to accurately model wavepacket motion. In terms of the KRR PES, the original, full kernel is able to capture couplings between all degrees-of-freedom; however, the large number of full-kernel functions required to adequately represent the PES with increasing dimensionality necessitated the introduction of the additive kernel highlighted above.[50] This additive kernel approach, in combination with SVD decomposition, provides an efficient route towards MCTDH propagation; however, as the truncation level of the kernel increases beyond second-order, to include three-mode couplings, the number of PES operator terms increases significantly, again introducing computational inefficiency.

In order to capture three-mode couplings, an extension of our second-order fitting procedure is required. In the case of second-order coupling, the two-dimensional PES operator terms were decomposed into a sum of outer-products of vectors along each degree-of-freedom; we wish to extend this concept to three-dimensional terms. To do so we have implemented a tensor decomposition algorithm which operates as follows

1. Perform the second-order SVD fitting, as described above.

2. For each triplet of degrees-of-freedom, construct a three-dimensional grid of geometries from the locations of the DVR points along each degree-of-freedom and evaluate the

19

KRR energy at each point, $V^{\mathrm{KRR}}(q_\lambda^l, q_\mu^m, q_\nu^n)$.

3. Construct the residual

$$
\begin{aligned}
V^{\lambda\mu\nu}(q_\lambda^l, q_\mu^m, q_\nu^n) = {}& V^{\mathrm{KRR}}(q_\lambda^l, q_\mu^m, q_\nu^n) - V^{\lambda\mu}(q_\lambda^l, q_\mu^m) - V^{\lambda\nu}(q_\lambda^l, q_\nu^n) - V^{\mu\nu}(q_\mu^m, q_\nu^n) \\
& - V^\lambda(q_\lambda^l) - V^\mu(q_\mu^m) - V^\mu(q_\mu^m) - V^{\mathrm{KRR}}(\mathbf{0}).
\end{aligned} \tag{21}
$$

4. Perform a tensor decomposition on the residual so that

$$
\mathbf{V}^{\lambda\mu\nu} \approx \tilde{\mathbf{V}}^{\lambda\mu\nu} = \sum_{j=1}^{\mathrm{R}_{\lambda\mu\nu}} \sigma_j \, \mathbf{V}^{\lambda\mu\nu}_{\lambda(j)} \otimes \mathbf{V}^{\lambda\mu\nu}_{\mu(j)} \otimes \mathbf{V}^{\lambda\mu\nu}_{\nu(j)} \tag{22}
$$

where the lth element of the vector $\mathbf{V}^{\lambda\mu\nu}_{\lambda(j)}$ is $V^{\lambda\mu\nu}_{\lambda(j)}(q_\lambda^l)$ and $\mathrm{R}_{\lambda\mu\nu}$ is the rank. Similar relations hold for the other two vectors in Eq. (22).

5. Repeat for all combination of three degrees-of-freedom.

The procedure we have implemented in step 4 is based upon the CANDECOMP/PARAFAC (CP) decomposition, where the final result is reached by an alternating least squares (ALS) algorithm.[59] The ALS algorithm minimises the norm, $||\mathbf{V}^{\lambda\mu\nu} - \tilde{\mathbf{V}}^{\lambda\mu\nu}||$ (defined analogously to the matrix Frobenius norm), by varying the terms along each degree-of-freedom one at a time while keeping the terms along the other two degrees-of-freedom constant. It should be noted that tensor decompositions used to produce the result in Eq. (22) have a rank $\mathrm{R}_{\lambda\mu\nu}$ which is generally unknown, but for practical reasons we assume here that the maximum rank is the minimum of the number of gridpoints along the three degrees-of-freedom.

To perform the decomposition in step 4, we define three matrices constructed from the vectors in Eq. (22), with $\mathbf{V}^{\lambda\mu\nu}_\Lambda = [\mathbf{V}^{\lambda\mu\nu}_{\lambda(1)} \cdots \mathbf{V}^{\lambda\mu\nu}_{\lambda(R_{\lambda\mu\nu})}]$, and similarly for $\mathbf{V}^{\lambda\mu\nu}_M$ and $\mathbf{V}^{\lambda\mu\nu}_N$. It is these matrices which are varied in each step of the optimisation of $||\mathbf{V}^{\lambda\mu\nu} - \tilde{\mathbf{V}}^{\lambda\mu\nu}||$. The optimisation proceeds as follows:

1. The first step is to matricise the residual tensor, $\mathbf{V}^{\lambda\mu\nu}$, with respect to each of its three modes.[59] The mode-n matricisation converts the tensor into a matrix where the

columns are the mode-n fibers of the tensor (rows, columns and tubes for modes 1,2 and 3 respectively). This process yields three matrices, $\mathbf{X}_{(1)}$, $\mathbf{X}_{(2)}$ and $\mathbf{X}_{(3)}$.

2. To initialise the matrices $\mathbf{V}_\Lambda^{\lambda\mu\nu}$, $\mathbf{V}_M^{\lambda\mu\nu}$ and $\mathbf{V}_N^{\lambda\mu\nu}$, the SVDs of the matrices $\mathbf{X}_{(i)}$ are performed and the $R_{\lambda\mu\nu}$ left singular vectors corresponding to the largest singular values are used as the first guesses for their respective matrices.

3. The first matrix to be varied is $\mathbf{V}_\Lambda^{\lambda\mu\nu}$ so calculate the $R_{\lambda\mu\nu} \times R_{\lambda\mu\nu}$ matrix

$$\mathbf{W}^\Lambda = (\mathbf{V}_M^{\lambda\mu\nu})^{\mathrm{T}}\mathbf{V}_M^{\lambda\mu\nu} * (\mathbf{V}_N^{\lambda\mu\nu})^{\mathrm{T}}\mathbf{V}_N^{\lambda\mu\nu} \tag{23}$$

where $*$ indicates the Hadamard product defined such that for the arbitrary matrices of the same dimensions, $\mathbf{C} = \mathbf{A} * \mathbf{B}$ is $C_{ij} = A_{ij}B_{ij}$.

4. Invert $\mathbf{W}^\Lambda$ and form the updated matrix

$$\tilde{\mathbf{V}}_\Lambda^{\lambda\mu\nu} = \mathbf{X}_{(1)}[\mathbf{V}_N^{\lambda\mu\nu} \odot \mathbf{V}_M^{\Lambda\mu\nu}](\mathbf{W}^\Lambda)^{-1} \tag{24}$$

where $\odot$ is the Khatri-Rao product defined as $\mathbf{C} = \mathbf{A} \odot \mathbf{B} = [\mathbf{a}_1 \circ \mathbf{b}_1 \cdots \mathbf{a}_R \circ \mathbf{b}_R]$. $\mathbf{a}_i$ and $\mathbf{b}_i$ are the ith columns of matrices $\mathbf{A}$ and $\mathbf{B}$ respectively and $\circ$ denotes the Kronecker product such that $\mathbf{a}_i \circ \mathbf{b}_i = (a_{1i}b_{1i}, a_{1i}b_{2i}, \cdots, a_{N_Ai}b_{N_Bi})^{\mathrm{T}}$.

5. The columns of $\tilde{\mathbf{V}}_\Lambda^{\lambda\mu\nu}$ are normalised with the normalisation coefficients forming the guess for the weights $\{\sigma_j\}$ in Eq. (22).

6. If any of the normalisation coefficients is less than 10^{-6}, the column is rejected and the rank, $R_{\lambda\mu\nu}$, reduced by one.

7. The previous four steps are repeated for the μ and ν components of the decomposition.

8. After all three degrees-of-freedom have been treated, $||\mathbf{V}^{\lambda\mu\nu} - \tilde{\mathbf{V}}^{\lambda\mu\nu}||$ is evaluated and if the norm is less than a pre-defined threshold or if it has changed by less than 10^{-6},

21

the optimisation is complete. Otherwise, the cycle repeats.

5.1 Application of tensor decomposition: malonaldehyde proton transfer

To test the tensor decomposition algorithm, calculations on the proton transfer in malonaldehyde were performed. Specifically, DD-SM calculations were performed in a three-dimensional subspace of the mass-frequency scaled normal modes of malonaldehyde centered at the proton transfer transition state geometry. The three modes chosen were labelled v_1 (proton transfer mode of frequency $1321.32\,\mathrm{cm}^{-1}$), v_{12} (out-of-plane proton motion with frequency $1290.31\,\mathrm{cm}^{-1}$) and v_{18} (OHO in-plane bending mode with frequency $1899.62\,\mathrm{cm}^{-1}$). These normal modes were calculated using the fitted PES of Mizukami *et al*,[60] which was also used for all potential evaluations in the wavepacket propagations. Along v_1 a 101 member sine DVR basis was used, with harmonic oscillator DVR bases used along v_{12} and v_{18}, both consisting of 21 functions. The initial wavefunction was centered at $v_1 = 0.5$ and $v_{12} = v_{18} = 0.0$, and was constructed of a three-dimensional Gaussian function of width $\langle \mathrm{d}q_i \rangle = 0.7$ in all directions. The dynamics were run for $100\,\mathrm{fs}$ using the 15th-order short iterative Lanczos integrator. In the first calculation, the PES was generated using the general kernel of Eq. (9), with the width parameter in Eq. (8) being $\alpha = 0.5$. KRR PES reference points were sampled every $1\,\mathrm{fs}$ within 3 wavefunction widths of the wavepacket center along each mode, with 100 geometries being chosen at each step; the PES was evaluated if the KRR variance exceeded 10^{-3}.

In addition to the standard KRR PES simulation, two new calculations were performed; the first proceeded with a PES operator built using the SVD fitting algorithm including sufficient terms to reduce the norm of the fitting residual (Eq. (20)) to $10^{-3}\mathrm{E_h}$. The second calculation used the same SVD fitting procedure, but also added third-order terms fitted using the tensor decomposition algorithm, the convergence criterion being the reduction of $||\mathbf{V}^{\lambda\mu\nu} - \tilde{\mathbf{V}}^{\lambda\mu\nu}||$ to $10^{-3}\,\mathrm{E_h}$.
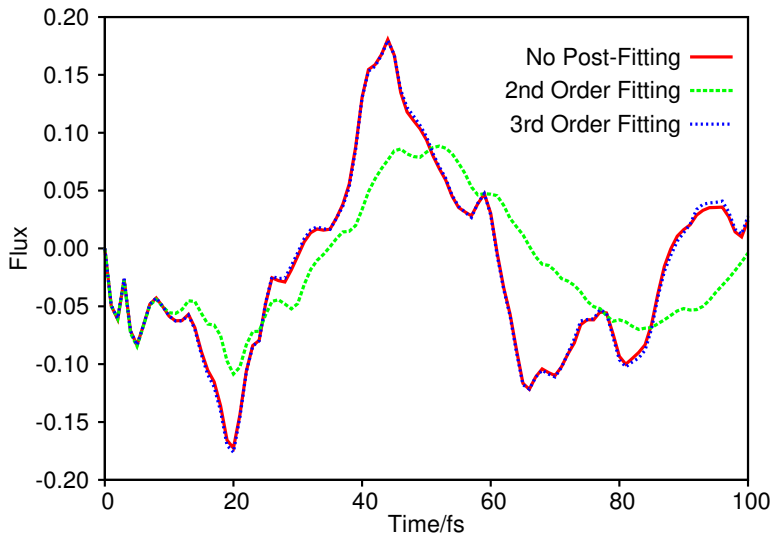
Figure 3: Wavefunction flux expectation values for proton transfer in a three-mode model of malonaldehyde. We illustrate the flux calculated using the raw KRR PES without further decomposition (red, solid line), using SVD decomposition of the KRR PES (green, dashed line), and using third-order terms constructed by tensor decomposition in addition to the second-order terms generated by SVD (blue, dashed line).

Figure 3 shows the wavefunction flux along the proton transfer coordinate in the three simulations. We obtain excellent agreement between the results produced using the KRR PES and that obtained when using third-order tensor decomposition. Clearly, truncating the potential fitting at second-order using the SVD algorithm results in very poor agreement with simulations performed on the full three-mode KRR PES representation. The RMSE (compared to the exact result) is 0.051, a factor of more than 7 larger than when third-order terms are included *via* tensor decomposition. A third-order decomposition of the full potential in this three-dimensional case should be exact, but the decomposition is the result of fitting to a sampled and hence imperfect potential, so exact agreement with the full potential should not be the expected result. However, the main conclusion is that little accuracy is lost by performing the secondary fitting.

It is worth noting that, while including three-mode coupling terms in the potential energy operator is vital to correctly model the wavepacket dynamics, the extra computational effort required is not insignificant. For example, we find that the addition of third-order terms

increases calculation time by about 33% (although the total required time is only 95 CPU seconds on a single processor). The reason for this increase is the larger total number of terms in the PES operator, which increases from 33 at second-order to 49 when including the tensor decomposition, leading to longer times for each step in the numerical integration of the equations-of-motion.

At this point, it is worth considering the relationship between the method proposed here and the well-established POTFIT method[17,45,46] for decomposing a general potential into sum-of-products form. POTFIT is based, as our method, upon a decomposition of the potential into a weighted sum of outer products of vectors along each degree-of-freedom (in POTFIT, referred to as single-particle potentials (SPPs)); the philosophies of the two methods are thus similar. Where the two methods differ is in which outer products are included. The POTFIT expansion includes all possible combinations of the SPPs; so, for a three-dimensional problem with 5 SPPs along each degree-of-freedom, there will be 25 terms in the POTFIT PES expansion (because a contraction along one of the degrees-of-freedom reduces the number from 125 to 25). To contrast, in our method, each vector along a degree-of-freedom only appears once. In addition, the POTFIT approach will only generate f-dimensional terms in the potential expansion for an f-dimensional problem, limiting its applicability when considering larger systems. Again, in contrast, our method restricts the dimensionality of the terms to 2 or 3, allowing easier treatment of larger systems, as demonstrated below.

To directly compare our method with POTFIT, we performed a series of three-dimensional decompositions of the malonaldehyde model potential using the POTFIT implementation in the Quantics package.[53] We then performed wavefunction propagation on the resulting POTFIT PESs using an identical dynamics setup as the calculations described in Fig. 3. Contraction of the POTFIT expansion coefficients was performed in the v_1 mode (as it requires the largest DVR basis), while the numbers of SPPs used along modes v_{12} and v_{18} was increased to improve the POTFIT PES accuracy. Comparing the resulting time-dependent

flux to the exact result (Fig. 3), we found that it was necessary to use 10 SPPs along each mode before the RMSE between calculated and exact flux (across the whole simulated time-scale) was lower than the calculated RMSE of our tensor expansion (RMSE = 0.0056 with 10 SPPs and RMSE = 0.0079 with 9 SPPs with RMSE = 0.0070 for our new tensor expansion). Using 10 SPPs along each mode creates a POTFIT expansion with 100 terms while our tensor expansion only used 49. As a result, we see that although our approach and POTFIT are similar in spirit, the different treatment of coupled degrees-of-freedom results in computational savings in terms of the number of terms in the resulting PES expansions; this, in turn, has an important effect on the efficiency of MCTDH propagations on these PESs.

6   Projection Diabatisation

In our previous work on DD-GB methods, when considering non-adiabatic dynamics *i.e.* problems involving multiple, coupled electronic states, we have used the propagation diabatisation scheme, originally proposed by one of us in the context of DD-vMCG method,[33,61] to produce the quasi-diabatic PESs. However, in performing DD-GB calculations using the propagation diabatisation method, we have come to realise that this approach is not well-suited to our on-the-fly KRR PES generation scheme. In this Section, we outline why this is the case and explore an alternative diabatisation scheme.

The propagation diabatisation method relies on the propagation of the adiabatic-diabatic transformation matrix along a straight line path in configuration space between two points where the adiabatic energies have been calculated at the complete active-space self consistent field (CASSCF) level. To do so the approximate relation

$$\nabla \mathbf{S} \approx -\underline{\mathbf{F}}\mathbf{S} \tag{25}$$

is used, which allows the transformation matrix, $\mathbf{S}$, to be determined at the end point of

the path by integrating the non-adiabatic coupling terms (NACTs), $\underline{\mathbf{F}}$ along that path. To achieve this, one must evaluate integrals of the following form:

$$\int_{\mathbf{q_a}}^{\mathbf{q_b}} \frac{\langle \psi_i | \nabla \hat{H}_{el} | \psi_j \rangle}{E_j - E_i} \cdot \mathrm{d}\mathbf{q} \tag{26}$$

where E_i and E_j are the adiabatic energies of electronic states ψ_i and ψ_j respectively. In practice this integral is calculated by evaluating the energies and NACTs at the start and end points of the path, $\mathbf{q_a}$ and $\mathbf{q_b}$. A KRR interpolation is carried out on all adiabatic energies in the database of saved energies to get a global representation of the adiabatic PESs. The trapezium rule is then used to calculate the value of the integral; derivative couplings at intermediate points are calculated from a linear interpolation between the known values in the KRR database, while the adiabatic energies are calculated from the KRR fit.[51]

The gauge of the adiabatic-diabatic transformation (which can be freely chosen) is set by defining $\mathbf{S}$ as the unit matrix at the centre of the nuclear wavepacket at $t = 0$. Because Eq. (25) is an approximation, and because we also evaluate Eq. (26) by an approximate interpolation scheme, it is not possible to get perfectly accurate diabatic PESs within this gauge (or any other) by using the propagation diabatisation scheme. In particular, while interpolation of the numerator is often a good approximation, the same is not true for the denominator or the individual, adiabatic energies from which it is constructed. At points of degeneracy, the denominator clearly causes a pole in the integrand, whilst in regions of space close to the degeneracy the approaching adiabatic PESs change rapidly.

This challenge is more clearly illustrated in Fig. 4, where it is assumed that $\mathbf{q}_a$ and $\mathbf{q}_b$ are two points (close to a degeneracy) between which we must integrate Eq. (26). Although we can evaluate the adiabatic energies at these end-points, we have no knowledge of the values of the potentials *between* these points. As a result, approximating the adiabatic PESs between the two points using an interpolation scheme such as KRR (or even just a simple linear interpolation) will give in an inaccurate representation of the energy gap, hence of

26

the integral in Eq. (26) and, consequently, of the diabatic potential at $\mathbf{q_b}$. This situation could be improved by performing evaluations of the adiabatic energies and NACTs at points intermediate between $\mathbf{q}_a$ and $\mathbf{q}_b$, but the additional computational expense is undesirable. It is also worth noting that the implementation of propagation diabatisation in the context of DD-vMCG does not suffer from this interpolation error to the same extent; in that case, the use of a local harmonic approximation to the PES, and the availability of first- and second-derivative information at $\mathbf{q}_a$ and $\mathbf{q}_b$, makes the propagation diabatisation method more reliable compared to our KRR interpolation scheme.
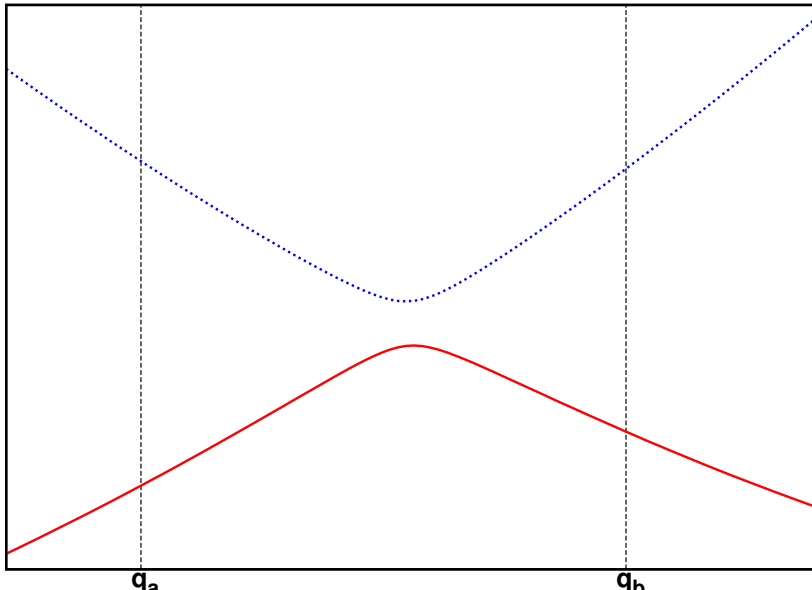

Figure 4: Illustration of a path between two points in configuration space, $\mathbf{q_a}$ and $\mathbf{q_b}$, close to a point of degeneracy, along which the non-adiabatic coupling must be integrated in order to diabatise the PESs using the propagation diabatisation scheme.

As a result of the incompatibility between DD-GB methods and the propagation diabatisation scheme, it is clear that a a different diabatisation scheme is preferred, particularly one which only requires adiabatic energy information and which is not reliant on path integration. One of us has recently developed such a method, referred to here as the projection diabatisation scheme.[62] The scheme highlighted here is along similar lines to that of Domcke and Woywod,[63] exploiting rotations on the orbitals and CI vectors of a CAS wavefunction to maximise overlap with a reference set of states. The current scheme generalises the approach

27

and is able to disentangle a manifold of diabatic states from a much larger set of adiabatic states exhibiting a large number of crossings and strong couplings.

Further details are given in Ref. 62, with algorithmic details outlined in the *Supplementary Information*. In the remainder of this section, we compare and contrast this new projection diabatisation to our original propagation diabatisation method.

6.1 Application to butatriene cation population transfer

The projection diabatisation scheme outlined in Ref. 62 has previously been applied to the evaluation of diabatic state energies for LiF and nitrogen oxide interacting with small gold clusters. To test the new diabatisation scheme within the context of the DD-GB method, we study the internal conversion occurring after excitation to the D_1 state of the butatriene cation. The geometry of the neutral molecule was optimised on the electronic ground state using the CASSCF method with an active space consisting of the three π and three π^* orbitals, occupied by six electrons. This CASSCF(6,6) calculation used a 3-21G basis set and, following geometry optimisation, a frequency calculation was performed to obtain the normal modes to be used in the dynamics calculation.

We first confirm that the new projection diabatisation scheme is capable of correctly capturing the behaviour of electronic states near avoided crossings. Here, two one-dimensional DD-SM calculations were performed using the four lowest energy electronic states of the butatriene cation, for the $14A_g$ normal mode (symmetric stretching of the central C=C bond, neutral ground state of $2195.19\,\mathrm{cm}^{-1}$). The wavepacket was propagated for 100 fs using 15th-order short iterative Lanczos integrator. A sine DVR basis with 81 members in $[-8, 8]$ along $14A_g$ was used. The initial wavepacket was a Gaussian function of width 0.7071 centered at the coordinate origin (corresponding to the Franck-Condon point) and placed on the first excited cation state (in the adiabatic representation, state D_1, and in the diabatic, $\tilde{A}$). During propagation, a KRR PES (with width parameter $\alpha = 0.05$) was generated by selecting up to 20 geometries (and their symmetry equivalent partners) every 1 fs, each of which was

added to the potential database if $\sigma^2(\mathbf{q}) > 10^{-3}$. Electronic structure calculations were performed at the state-averaged (SA) CASSCF(5,6)/3-21G level using Molpro.[64–66] These above conditions were the same for each of the two calculations performed, with the only difference between the two being the method of diabatisation.

Figure 5 shows the potential energy curves for the two lowest energy states obtained during both calculations. Examining the results obtained using the projection diabatisation scheme in Fig. 5(a); near $q_{14} = 1.8$, we see evidence of the well-known avoided crossing in the two lowest-energy ion states of butatriene (seen as a conical intersection in higher-dimensions). Clearly the adiabatic curves approach one another before diverging again. In the diabatic representation we expect to see two curves crossing, and this is indeed the case here; to the left of the avoided crossing the D_0 adiabatic and $\tilde{X}$ diabatic states correspond, whilst to the right the $\tilde{A}$ diabat becomes associated with the D_0 state. The opposite picture is seen for the D_1 state. In Fig. 5(b), illustrating the results of the simulation perform with propagation diabatisation, we do not see the crossing of the diabats; the $\tilde{X}$ diabat corresponds to the D_0 adiabatic state across the full domain (likewise for $\tilde{A}$ and D_1), despite the presence of the avoided crossing being easily inferred from the shapes of the curves. As noted in the previous section, this clearly justifies using the projection diabatisation scheme in DD-GB simulations (where no derivative information is used, as it is in DD-vMCG). We note that we have performed a similar analysis of the diabatic states generated using the projection diabatisation scheme for two-dimensional sections through the butatriene state manifold; further details are given in the *Supplementary Information*.

To further verify the physical nature of the projection diabatisation scheme, Fig. 6 shows the geometry-dependence of the diabatic coupling term, given by KRR fitting, between the D_0 and D_1 states which was generated by the four-state calculation. We find that the coupling varies in an approximately linear fashion along the $5A_u$ mode. Satisfyingly, this is to be expected, as explained previously;[67] butatriene has D_{2h} symmetry and the D_0 and D_1 cation states are in the B_{2g} and B_{2u} irreducible representations, respectively. It follows that
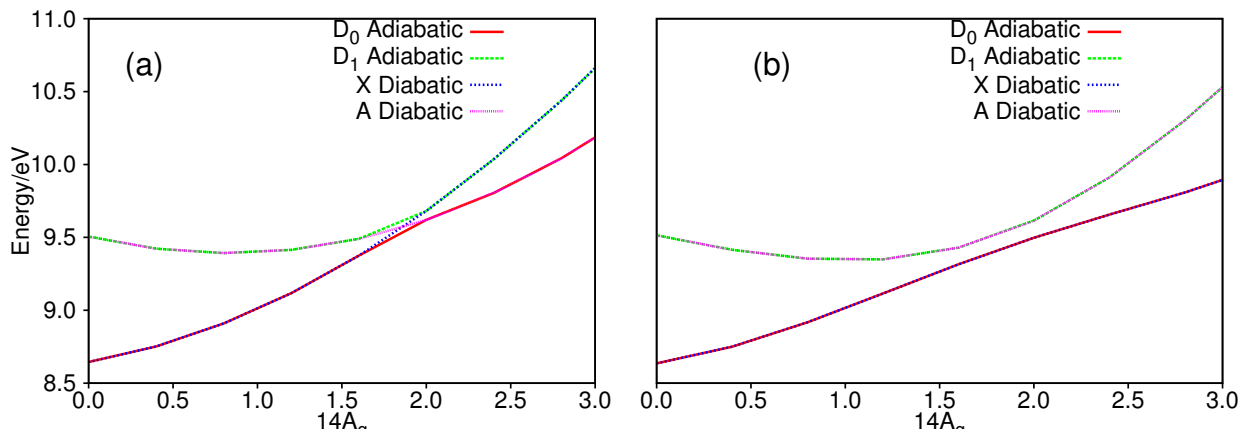
Figure 5: The 2 lowest-energy potential energy curves of the butatriene cation as a function of the $14A_g$ (symmetric stretch of central CC bond) mass-frequency scaled normal mode. (a) Adiabatic and diabatic curves calculated using the projection diabatisation scheme. (b) Adiabatic and diabatic curves calculated using the propagation diabatisation scheme.

interstate coupling is non-zero only if the direct product of the state symmetries and the coupling operator includes the totally symmetric representation. As a result, the coupling operator must have A_u symmetry hence, to a first-order approximation, the coupling should be of the form $\lambda\langle\psi_{D_0}|q_5|\psi_{D_1}\rangle$ where λ is some constant. Our results agree with that analysis, indicating that the projection diabatisation scheme reproduces the coupling expected on symmetry grounds.

Finally, to highlight the fact that projection diabatisation enables smooth wavefunction propagation, in Fig. 7 we illustrate the wavepacket population of the $\tilde{A}$ diabatic state obtained in DD-SM calculations on KRR PESs using projection diabatisation. The populations of the $\tilde{B}$ and $\tilde{C}$ states were negligible during the course of the four-state propagation (as expected by their higher energies relative to the Franck-Condon point on $\tilde{A}$). In addition, Fig. 7 also shows the population of the $\tilde{A}$ state calculated in our earlier work[51] using a previously published, two-state VCHAM potential[67] in order for a qualitative comparison to be made. This fitted VCHAM potential uses a proper torsion coordinate as a degree-of-freedom, rather than the $5A_u$ normal-mode used in the DD-SM calculations, so comparisons between the two sets will not be exact but are the best available. Similar plots were pre-
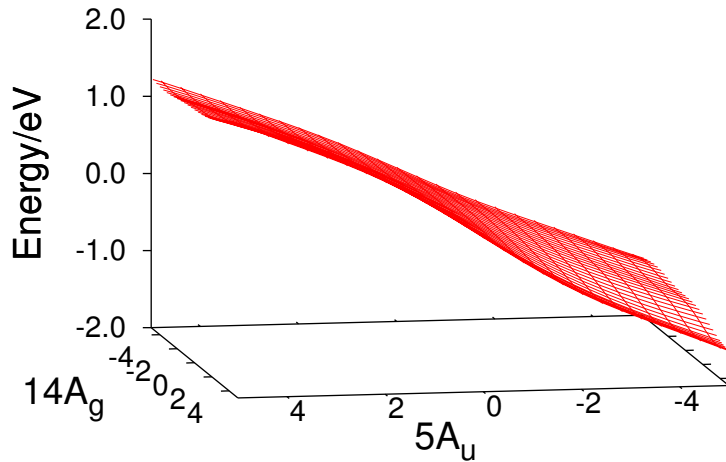
Figure 6: KRR fit of the diabatic coupling between the $\tilde{X}$ and $\tilde{A}$ states of butatriene as a function of mass-frequency scaled normal mode coordinates.

sented in previous work where the dynamics of the butatriene cation were studied: in Ref. 67 surface hopping dynamics were performed; in Ref. 68 MCTDH calculation on vibronic coupling Hamiltonian fitted PES were performed; in Ref. 69 DD-vMCG was used together with a regularisation diabatisation scheme, whilst in Refs. 33 and 61 DD-vMCG coupled to the propagation diabatisation scheme was used. With the exception of Ref. 61, all of these calculations were carried out using only two electronic states. Referring back to these earlier works, and comparing to the blue, dashed line in Fig. 7 we see the same qualitative behaviour in the population transfer with immediate, rapid depopulation of the $\tilde{A}$ diabatic state as the wavepacket reaches the location of the $\tilde{X}/\tilde{A}$ surface crossing followed by a partial re-population between 10 and 20 fs as the wavepacket reverses along the $14A_g$ mode. In all cases a further depopulation occurs up to 30 fs before rebounding again. However, at this point there is a divergence between the VCHAM and DD-SM results; the VCHAM plot exhibits a triplet-like feature between 40 and 60 fs, which is also seen in the DD-SM cases but only after a further depopulation and re-population cycle between 40 and 50 fs. The

two DD-SM results differ because of the different levels of electronic structure theory used to calculate the potentials *i.e.* in the number of states over which the CASSCF was state-averaged, but the results are still qualitatively the same. We find that the time-dependent population is very similar to previous work performed with comparable levels of electronic structure calculations; as a result, we conclude that the diabatisation scheme outlined here qualitatively reproduces the results of previous simulations but, crucially, requires neither evaluation of non-adiabatic coupling matrix elements nor full PES fitting.
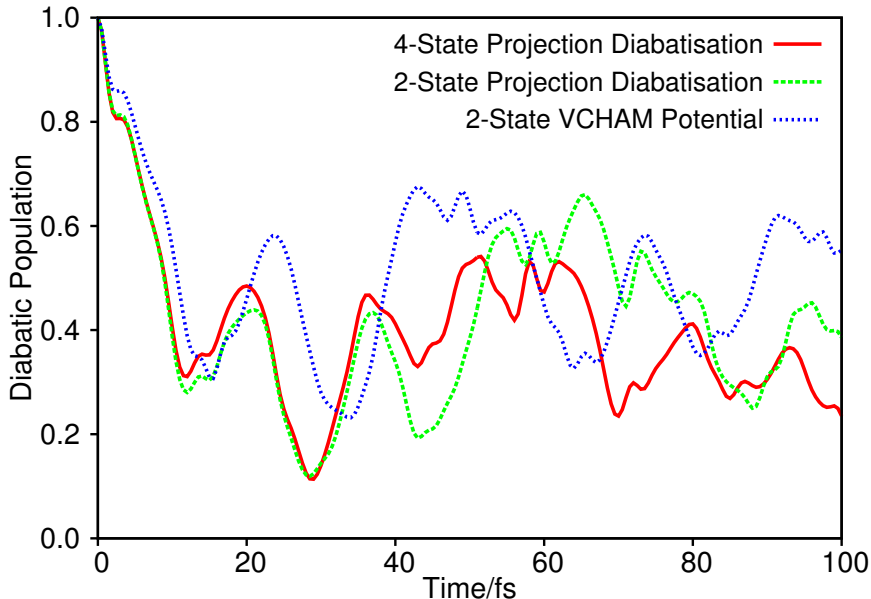

Figure 7: Population of the first excited diabatic state, $\tilde{A}$, of the butatriene cation as a function of propagation time. The red, solid line is the result obtained using the projection diabatisation scheme, outlined here, on four electronic states, the green, hashed line is the result of using DD-SM propagation on two states diabatised using the projection diabatisation scheme. The blue, dashed line is the result of a calculation performed on two VCHAM fitted potential energy surfaces (modified from Ref. 51).

Considering the results from the one- and two-dimensional PES construction (see *Supplementary Information*), as well as the qualitative reproduction of the diabatic-state population dynamics when compared to previous work, it is clear that the new projection diabatisation scheme is a very useful addition to the DD-GB method. It has a less rigorous background than the propagation diabatisation scheme implemented originally, but is less computationally demanding, requiring only electronic energy evaluations with no need to

calculate non-adiabatic coupling vectors between all pairs of states.

7 Non-Adiabatic Dynamics of Pyrazine

In the previous sections, we have highlighted four algorithmic and methodological improvements which we have proposed as part of a DD-GB scheme for quantum dynamics. To bring together all of these developments, the final Section of this article shows how we can perform a direct MCTDH simulation of a many-dimensional, non-adiabatic system using *ab initio* electronic structure evaluations of the adiabatic state energies within a reasonable timeframe and without pre-fitting of a PES. To this end, we return to the classic example of the photo-initiated dynamics of pyrazine.

The geometry of pyrazine was optimised on the electronic ground state using the SA-CASSCF(10,8)/DZP level in Molpro, the averaging being equal over three states and the active space comprising the six orbitals in the π-system along with the two, non-bonding lone pair orbitals on the nitrogen atoms. We selected 12 mass-frequency-scaled normal modes as active vibrational coordinates, and DD-MCTDH calculations were performed using the two excited states, S_1 and S_2. The *Supplementary Information* gives details of the normal modes, as well as the number of DVR gridpoints (all modes used a harmonic oscillator basis), mode combinations and number of SPFs used in each state.[70] The initial wavefunction was a 12-dimensional product of ground-state harmonic oscillator eigenfunction centered at the coordinate origin on the S_2 state (the Franck-Condon point). Time-propagation was performed for 100 fs. Reference geometries for the KRR PES were generated using Sobol sequence sampling, the space sampled being within three widths of the wavepacket center along each mode, every 1 fs; 10^3 geometries were generated at each step, and were accepted for energy evaluation if $\sigma^2(\mathbf{q}) > 10^{-3}$ (Eq. (14)). Electronic structure calculations were performed using the same level as used to optimise the geometry, with the orbitals subsequently diabatised in Molpro by maximising the overlap with the orbitals at the reference,

Franck-Condon geometry, and the 20 lowest energy states calculated without further orbital optimisation. The resulting energies were then diabatised as described above. The KRR PES was fitted using a third-order additive kernel, the width parameter of the Gaussian functions being $\alpha = 0.01$. During this initial wavefunction propagation, a secondary fitting of the PES to second-order was performed, with the residual threshold (Eq. (20)) being 10^{-3} E$_h$.

After initial propagation, which generated a database of 2744 reference geometries, two further calculations were performed using the same database to construct the PES. The first of these simply used the same initial conditions as the original calculation, but without any further sampling of configuration space, whilst the second calculation included fitting of the PES to third-order using the tensor decomposition method with convergence threshold of 10^{-3} E$_h$.

Figure 8 presents the results of these calculations on pyrazine; to date, these are the largest simulations which have been performed using our DD-MCTDH methodology. Figure 8(a) shows the absorption spectra calculated after each propagation by performing a Fourier transform on the autocorrelation function $(c(t) = \langle \Psi(0) | \Psi(t) \rangle)$ with a damping time of $50 \, \text{fs}$ (for full details see Ref. 17). Clearly the spectra are very similar, with the small differences observed caused by the different structure of each PES; during the first run, the shape of the PES changes as each new point is added to the database, whereas the calculations performed subsequently used a static PES database. Clearly, the difference between the read-only second- and third-order simulations is very small, suggesting that two-mode coupling effects account for the dominant dynamics in this particular case. All three spectra in Fig. 8(a) compare well with that calculated earlier using MCTDH and a pre-fitted PES;[70] the overall shapes are similar, although there are differences in the pattern of peaks on the low energy side. Such differences are to be expected because the PES are calculated using very different methods; the fitted surface from the earlier work was constructed using data from MP2, CIS, CASSCF and MRCI electronic structure calculations, whereas this work used CASSCF (and a modest basis set) only. The spectra also compare well to the experimental

results in Ref. 71; the overall shape is similar in particular the peaks between 6.0 and 6.3 eV and the long tail at high energy. The total widths are also comparable being just over 1.0 eV in the experiment and about 1.2 eV here.
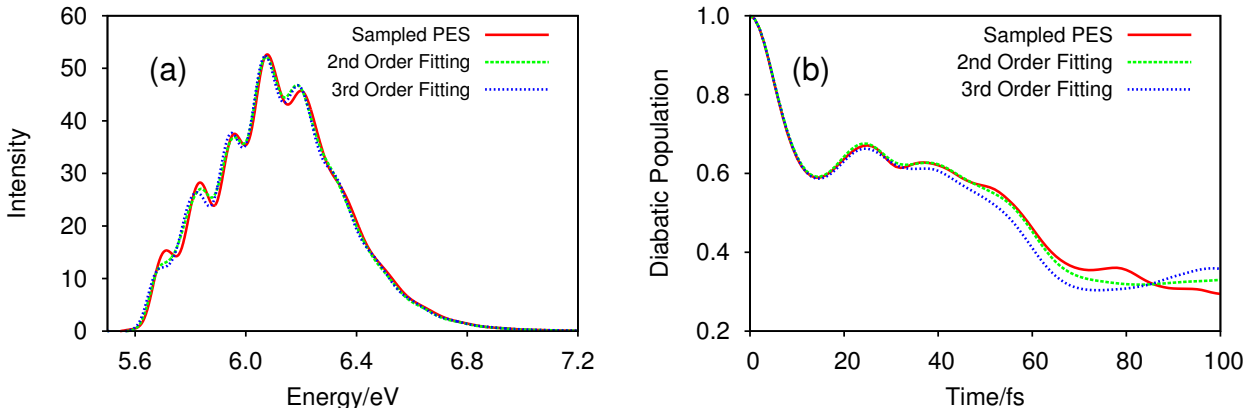

Figure 8: Results of wavepacket propagation on a 12-mode/2-state model of pyrazine using DD-MCTDH. (a) Absorption spectra upon vertical excitation to the S_2 electronic state. (b) Populations of the S_2 diabatic state. In both plots, results are shown for third-order additive kernel with SVD secondary fitting (red, solid line), a second calculation performed using the PES database generated in the first calculation, but without any further addition of PES database entries (green, dashed line), and a third calculation again using the PES database from the first calculation but using an additional third-order decomposition to generate the PES operator for MCTDH propagation (blue, dashed line).

Figure 8(b) shows the population of the S_2 diabatic state as a function of propagation time for all three calculations. The three plots agree very closely for the first 20 fs before slowly diverging for the same reasons as discussed above. The diabatic state populations diverge more at longer times; the similarity of the spectra in Fig. 8(a) is thus seen to be caused by the relatively short damping time when performing the Fourier transform; longer timescale differences in the dynamics are missed there. The actual population transfer is significant in all three calculations, starting immediately as the wavefunction encounters a crossing of the two diabatic states, rebounding partially at around 20-30 fs before beginning a slower transfer from S_2 to S_1. The extent of population transfer is not as significant as was seen in earlier studies using MCTDH on full, fitted PESs;[72,73] again, this is to be expected based on the different methods for PES construction.

As an aside, it is worth highlighting the fact that the results of Fig. 8 are well-converged with respect to the key simulation parameters of our direct MCTDH scheme. For example, in the *Supplementary Information*, we show results of repeated calculations, but with slightly increased numbers of SPFs in the MCTDH wavefunction, and different KRR width parameters employed in either SVD fitting (two-mode PES representation) or tensor decomposition (three-mode PES representation). In each case, we find minimal changes in the quantitative results, suggesting that the results of Fig. 8 represent converged results for the particular choice of electronic structure, number of modes and initial wavefunction.

To assess the accuracy of the KRR-generated PESs, 10^3 configurations were randomly generated by drawing samples randomly from the coordinate range sampled during the wavepacket evolution, then keeping those points which have calculated KRR variance less than 10^{-3} E_h. Here, 277 geometries were accepted based on the calculated variance, and the RMSE for these points relative to CASSCF calculations at the same geometries was found to be 2.39×10^{-2} E_h overall (including both electronic states). This error is a significant improvement over the equivalent results given in section IV.D in Ref. 50 for a 4-mode/2-state calculation on pyrazine, where the RMSE was 7.39×10^{-2} E_h. There we noted that the likely cause of the error was due to ignoring third-order terms and errors in the diabatisation scheme; it is therefore satisfying to see that improvements to these aspects have reduced PES errors, even when more degree-of-freedom are included.

Perhaps one of the most important conclusions of this work relates to the required computational time for these DD-MCTDH simulations. The initial calculation (three-body kernel and two-mode SVD decomposition) took just under 29 hours walltime on a standard desktop (including both the dynamics and all 2744 Molpro calculations). The second calculation using the pre-computed database with the PES fitted to second-order took $6\frac{1}{2}$ hours, whilst the calculation with PES decomposed to third-order took $61\frac{1}{2}$ hours; the increase in time here is due to the increased number of terms in the third-order PES decomposition. When compared to the cost of pre-computing and pre-fitting complex diabatic PESs, the ability to

run an initial DD-MCTDH calculation in just 29 hours is highly-encouraging; direct, on-the-fly MCTDH simulations of complex photodynamics now seem increasingly accessible, and there remain many opportunities for algorithm optimization.

8   Conclusions

In this work, we have presented four distinct algorithmic improvements to our DD-GB simulation approach; as highlighted above, these developments now enable direct non-adiabatic simulations using MCTDH for systems containing >10 vibrational coordinates in just a few hours on a standard desktop. We have shown how Cholesky update in the initial KRR fitting of the PES has allowed a large speed-up in these calculations, while the introduction of Sobol sampling has improved the repeatability of our simulations. We have also shown how our previous SVD method for generating efficient representations of the KRR PES can be expanded to account for three-mode couplings using tensor decomposition; we note that the same approach could, in principle, be expanded beyond three-mode coupling, albeit at additional computational expense. Finally, we have highlighted how a recently-developed projection diabatisation scheme can be used with our DD-MCTDH method; this provides a useful alternative diabatisation scheme, in addition to the original propagation diabatisation scheme which we have employed previously. Tests on several molecular systems have individually shown the efficiency of these improvements, whilst all were combined to allow the study of the non-adiabatic dynamics of pyrazine using a 12-dimensional model; this is an important advance in the capacity of DD-GB methods.

Promisingly, there are avenues which can be explored to further increase the efficiency of our DD methodology. For example, the question of how one selects the kernel width parameters has not been extensively discussed here; to address this, we note that we could employ Gaussian process regression instead of KRR, and optimise width parameters by maximisation of the log marginal likelihood. Other extensions of our DD-GB strategy include

incorporation of spin-orbit couplings, more effective treatment of molecular symmetry, and the use of coordinate systems other than normal modes to allow efficient treatment of, for example, cis-trans isomerisation. All of these directions are now in progress; however, the results presented here serve to show that our DD-MCTDH strategy is emerging as an efficient new route towards modelling quantum dynamics in complex molecular systems.

Acknowledgements

References

(1) Meyer, H.-D.; Manthe, U.; Cederbaum, L. The multi-configurational time-dependent Hartree approach. *Chem. Phys. Lett.* **1990**, *165*, 73 – 78.

(2) Raab, A.; Worth, G. A.; Meyer, H.-D.; Cederbaum, L. S. Molecular dynamics of pyrazine after excitation to the S2 electronic state using a realistic 24-mode model Hamiltonian. *J. Chem. Phys.* **1999**, *110*, 936 – 946.

(3) Burghardt, I.; Meyer, H.-D.; Cederbaum, L. S. Approaches to the approximate treatment of complex molecular systems by the multiconfiguration time-dependent Hartree method. *J. Chem. Phys.* **1999**, *111*, 2927–2939.

(4) Schröder, M.; Meyer, H.-D. Calculation of the vibrational excited states of malonaldehyde and their tunneling splittings with the multi-configuration time-dependent Hartree method. *J. Chem. Phys.* **2014**, *141*, 034116/1–13.

(5) Manthe, U. The multi-configuration time-dependent Hartree approach revisited. *J. Chem. Phys.* **2015**, *142*, 244109/1–15.

(6) Meyer, H.-D., Gatti, F., Worth, G. A., Eds. *Multidimensional quantum dynamics: MCTDH theory and applications*; Wiley: Weinheim, Germany, 2009.

(7) Dirac, P. Note on Exchange phenomena in the Thomas atom. *Proc. Cambridge Philos. Soc.* **1930**, *26*, 376–385.

(8) Frenkel, J. *Wave Mechanics*; Clarendon Press, Oxford, 1934.

(9) Broeckhove, J.; Lathouwers, L.; Kesteloot, E.; Van Leuven, P. On the equivalence of time-dependent variational principles. *Chem. Phys. Lett.* **1988**, *149*, 547–550.

(10) Wu, G.; Neville, S. P.; Schalk, O.; Sekikawa, T.; Ashfold, M. N. R.; Worth, G. A.; Stolow, A. Excited state non-adiabatic dynamics of N-methylpyrrole: A time-resolved photoelectron spectroscopy and quantum dynamics study. *J. Chem. Phys.* **2016**, *144*, 014309/1–12.

(11) Zheng, J.; Xie, Y.; Jiang, S.; Lan, Z. Ultrafast Nonadiabatic Dynamics of Singlet Fission: Quantum Dynamics with the Multilayer Multiconfigurational Time-Dependent Hartree (ML-MCTDH) Method. *J. Phys. Chem. C* **2016**, *120*, 1375–1389.

(12) Meng, Q.; Meyer, H.-D. A multilayer MCTDH study on the full dimensional vibronic dynamics of naphthalene and anthracene cations. *J. Chem. Phys.* **2013**, *138*, 014313/1–12.

(13) Füchsel, G.; Thomas, P. S.; den Uyl, J.; Öztürk, Y.; Nattino, F.; Meyer, H.-D.; Kroes, G.-J. Rotational effects on the dissociation dynamics of CHD3 on Pt(111). *Phys. Chem. Chem. Phys.* **2016**, *18*, 8174–8185.

(14) Firmino, T.; Marquardt, R.; Gatti, F.; Dong, W. Diffusion Rates for Hydrogen on Pd(111) from Molecular Quantum Dynamics Calculations. *J. Phys. Chem. Lett.* **2014**, *5*, 4270–4274.

(15) Fumanal, M.; Plasser, F.; Mai, S.; Daniel, C.; Gindensperger, E. Interstate vibronic coupling constants between electronic excited states for complex molecules. *J. Chem. Phys.* **2018**, *148*, 124119.

(16) Fumanal, M.; Gindensperger, E.; Daniel, C. Ultrafast Excited-State Decays in [Re(CO)3(N,N)(L)]n+: Nonadiabatic Quantum Dynamics. *J. Chem. Theory Comput.* **2017**, *13*, 1293–1306.

(17) Beck, M. H.; Jäckle, A.; Worth, G. A.; Meyer, H. D. The Multiconfiguration Time-Dependent Hartree (MCTDH) Method: A Highly Efficient Algorithm For Propagating Wavepackets. *Phys. Rep.* **2000**, *324*, 1–105.

(18) Wang, H.; Thoss, M. Multilayer formulation of the multiconfiguration time-dependent Hartree theory. *J. Chem. Phys.* **2003**, *119*, 1289–1299.

(19) Vendrell, O.; Meyer, H.-D. Multilayer multiconfiguration time-dependent Hartree method: Implementation and applications to a Henon-Heiles Hamiltonian and to pyrazine. *J. Chem. Phys.* **2011**, *134*, 044135/1–16.

(20) Wang, H. Multilayer Multiconfiguration Time-Dependent Hartree Theory. *J. Phys. Chem. A* **2015**, *119*, 7951–7965.

(21) Li, J.; Kondov, I.; Wang, H.; Thoss, M. Quantum dynamical simulation of photoinduced electron transfer processes in dye–semiconductor systems: theory and application to coumarin 343 at TiO2. *J. Phys.: Condens. Matter* **2015**, *27*, 134202/1–13.

(22) Martinez, T. J.; Ben-Nun, M.; Levine, R. D. Multi-Electronic-State Molecular Dynamics: A Wave Function Approach with Applications. *J. Phys. Chem.* **1996**, *100*, 7884–7895.

(23) Ben-Nun, M.; Quenneville, J.; Martínez, T. J. Ab Initio Multiple Spawning: Photochemistry from First Principles Quantum Molecular Dynamics. *J. Phys. Chem. A* **2000**, *104*, 5161–5175.

(24) Virshup, A. M.; Punwong, C.; Pogorelov, T. V.; Lindquist, B. A.; Ko, C.; Martínez, T. J. Photodynamics in Complex Environments: Ab Initio Multiple Spawning Quantum Mechanical/Molecular Mechanical Dynamics. *J. Phys. Chem. B* **2009**, *113*, 3280–3291.

(25) Ben-Nun, M.; Martínez, T. J. Nonadiabatic molecular dynamics: Validation of the multiple spawning method for a multidimensional problem. *J. Chem. Phys.* **1998**, *108*, 7244–7257.

(26) Martinez, T. J.; Levine, R. D. Non-adiabatic molecular dynamics: Split-operator multiple spawning with applications to photodissociation. *J. Chem. Soc., Faraday Trans.* **1997**, *93*, 941–947.

(27) Ben-Nun, M.; Martinez, T. J. Ab initio quantum molecular dynamics. *Adv. Chem. Phys.* **2002**, *121*, 439–512.

(28) Saller, M. A. C.; Habershon, S. Quantum Dynamics with Short-Time Trajectories and Minimal Adaptive Basis Sets. *J. Chem. Theory Comput.* **2017**, *13*, 3085–3096.

(29) Alborzpour, J. P.; Tew, D. P.; Habershon, S. Efficient and accurate evaluation of potential energy matrix elements for quantum dynamics using Gaussian process regression. *J. Chem. Phys.* **2016**, *145*, 174112/1–11.

(30) Saller, M. A. C.; Habershon, S. Basis Set Generation for Quantum Dynamics Simulations Using Simple Trajectory-Based Methods. *J. Chem. Theory Comput.* **2015**, *11*, 8–16.

(31) Habershon, S. Path integral density matrix dynamics: A method for calculating time-dependent properties in thermal adiabatic and non-adiabatic systems. *J. Chem. Phys.* **2013**, *139*, 104107/1–11.

(32) Habershon, S. Linear dependence and energy conservation in Gaussian wavepacket basis sets. *J. Chem. Phys.* **2012**, *136*, 014109/1–8.

(33) Richings, G.; Worth, G. A Practical Diabatisation Scheme for Use with the Direct-Dynamics Variational Multi-Configuration Gaussian Method. *J. Phys. Chem. A* **2015**, *119*, 12457–12470.

(34) Mendive-Tapia, D.; Lasorne, B.; Worth, G.; Robb, M.; Bearpark, M. Towards converging non-adiabatic direct dynamics calculations using frozen-width variational Gaussian product basis functions. *J. Chem. Phys.* **2012**, *137*, 22A548/1–10.

(35) Worth, G. A.; Robb, M. A. Applying direct molecular dynamics to non-adiabatic systems. *Adv. Chem. Phys.* **2002**, *124*, 355–432.

(36) Worth, G. A.; Robb, M. A.; Lasorne, B. Solving the time-dependent Schrödinger Equation in one step: Direct Dynamics of Non-adiabatic Systems. *Mol. Phys.* **2008**, *106*, 2077–2091.

(37) Shalashilin, D. V. Quantum mechanics with the basis set guided by Ehrenfest trajectories: Theory and application to spin-boson model. *J. Chem. Phys.* **2009**, *130*, 244101/1–11.

(38) Sherratt, P. A.; Shalashillin, D. V.; Child, M. S. Description of multidimensional tunnelling with the help of coupled coherent states guided by classical Hamiltonians with quantum corrections. *Chem. Phys.* **2006**, *322*, 127–134.

(39) Shalashilin, D. V. Nonadiabatic dynamics with the help of multiconfigurational Ehrenfest method: Improved theory and fully quantum 24D simulation of pyrazine. *J. Chem. Phys.* **2010**, *132*, 244111/1–11.

(40) Shalashilin, D. V.; Child, M. S. Basis set sampling in the method of coupled coherent states: Coherent state swarms, trains, and pancakes. *J. Chem. Phys.* **2008**, *128*, 054102/1–6.

(41) Koch, W.; Frankcombe, T. J. Basis Expansion Leaping: A New Method to Solve the Time-Dependent Schrödinger Equation for Molecular Quantum Dynamics. *Phys. Rev. Lett.* **2013**, *110*, 263202/1–5.

(42) Levine, B. G.; Coe, J. D.; Virshup, A. M.; Martínez, T. J. Implementation of ab initio multiple spawning in the Molpro quantum chemistry package. *Chem. Phys.* **2008**, *347*, 3–16.

(43) Cederbaum, L. S.; Köppel, H.; Domcke, W. Multimode vibronic coupling effects in molecules. *Int. J. Quant. Chem.* **1981**, *15*, 251–267.

(44) McKinlay, R. G.; Żurek, J. M.; Paterson, M. J. In *Theoretical and Computational Inorganic Chemistry*; van Eldik, R., Harvey, J., Eds.; Advances in Inorganic Chemistry; Academic Press, 2010; Vol. 62; pp 351 – 390.

(45) Jäckle, A.; Meyer, H.-D. Product representation of potential energy surfaces. *J. Chem. Phys.* **1996**, *104*, 7974–7984.

(46) Peláez, D.; Meyer, H.-D. The multigrid POTFIT (MGPF) method: Grid representations of potentials for quantum dynamics of large systems. *J. Chem. Phys.* **2013**, *138*, 014108/1–16.

(47) Manthe, U. A time-dependent discrete variable representation for (multiconfiguration) Hartree methods. *J. Chem. Phys.* **1996**, *105*, 6989–6994.

(48) Wodraszka, R.; Carrington, T. A new collocation-based multi-configuration time-dependent Hartree (MCTDH) approach for solving the Schrödinger equation with a general potential energy surface. *J. Chem. Phys.* **2018**, *148*, 044115/1–11.

(49) Richings, G.; Habershon, S. Direct Quantum Dynamics Using Grid-Based Wave Function Propagation and Machine-Learned Potential Energy Surfaces. *J. Chem. Theory Comput.* **2017**, *13*, 4012–4024.

(50) Richings, G.; Habershon, S. MCTDH on-the-fly: Efficient grid-based quantum dynamics without pre-computed potential energy surfaces. *J. Chem. Phys.* **2018**, *148*, 134116/1–13.

(51) Richings, G.; Habershon, S. Direct grid-based quantum dynamics on propagated diabatic potential energy surfaces. *Chem. Phys. Lett.* **2017**, *683*, 228–233.

(52) Williams, C. In *Handbook of Brain Theory and Neural Networks*; Arbib, M., Ed.; The MIT Press: Cambridge, Massachusetts, 2002; pp 466–470.

(53) Worth, G.; Giri, K.; Richings, G.; Burghardt, I.; Beck, M.; Jäckle, A.; Meyer, H.-D. *The Quantics Package, Version 1.1*; 2016.

(54) Osborne, M. A.; Rogers, A.; Ramchurn, S.; Roberts, S. J.; Jennings, N. R. Towards Real-Time Information Processing of Sensor Network Data using Computationally Efficient Multi-output Gaussian Processes. International Conference on Information Processing in Sensor Networks (IPSN 2008). 2008; pp 109–120, Event Dates: April 2008.

(55) Sobol, I. Distribution of points in a cube and approximate evaluation of integrals. *USSR Comput. Maths. Math. Phys.* **1967**, *7*, 86–112.

(56) Rabitz, H.; Aliş, O. General foundations of high-dimensional model representations. *J. Math. Chem.* **1999**, *25*, 197–233.

(57) Aliş, O.; Rabitz, H. Efficient implementation of high dimensional model representations. *J. Math. Chem.* **2001**, *29*, 127–142.

(58) Ho, T.-S.; Rabitz, H. Reproducing kernel Hilbert space interpolation methods as a paradigm of high dimensional model representations: Application to multidimensional potential energy construction. *J. Chem. Phys.* **2003**, *119*, 6433–6442.

(59) Kolda, T. G.; Bader, B. W. Tensor Decomposition and Applications. *SIAM Rev.* **2009**, *51*, 455–500.

(60) Mizukami, W.; Habershon, S.; Tew, D. A compact and accurate semi-global potential energy surface for malonaldehyde from constrined least squares regression. *J. Chem. Phys.* **2014**, *141*, 144310/1–9.

(61) Richings, G.; Worth, G. Muti-state non-adiabatic direct-dynamics on propagated diabatic potential energy surfaces. *Chem. Phys. Lett.* **2017**, *683*, 606–612.

(62) Robertson, C.; Gonzalez-Vazquez, J.; Diaz-Tendero, S.; Corral, I.; Diaz, C. *J. Comp. Chem.* **2018**, (in press).

(63) Domcke, W.; Woywod, C. Direct construction of diabatic states in the CASSCF approach. Application to the conical intersection of the 1A2 and 1B1 excited states of ozone. *Chem. Phys. Lett.* **1993**, *216*, 362–368.

(64) Werner, H.-J.; Knowles, P. J.; Knizia, G.; Manby, F. R.; Schütz, M.; Celani, P.; Györffy, W.; Kats, D.; Korona, T.; Lindh, R.; Mitrushenkov, A.; Rauhut, G.; Shamasundar, K. R.; Adler, T. B.; Amos, R. D.; Bernhardsson, A.; Berning, A.; Cooper, D. L.; Deegan, M. J. O.; Dobbyn, A. J.; Eckert, F.; Goll, E.; Hampel, C.; Hesselmann, A.; Hetzer, G.; Hrenar, T.; Jansen, G.; Köppl, C.; Liu, Y.; Lloyd, A. W.; Mata, R. A.; May, A. J.; McNicholas, S. J.; Meyer, W.; Mura, M. E.; Nicklass, A.; O'Neill, D. P.; Palmieri, P.; Peng, D.; Pflüger, K.; Pitzer, R.; Reiher, M.; Shiozaki, T.; Stoll, H.; Stone, A. J.; Tarroni, R.; Thorsteinsson, T.; Wang, M. MOLPRO, version 2010.1, a package of ab initio programs. 2010; www.molpro.net.

(65) Werner, H.-J.; Knowles, P. J. A Second Order MCSCF Method with Optimum Convergence. *J. Chem. Phys.* **1985**, *82*, 5053–5063.

(66) Knowles, P. J.; Werner, H.-J. An efficient second-order MC SCF method for long configuration expansions. *Chem. Phys. Lett.* **1985**, *115*, 259–267.

(67) Worth, G.; Hunt, P.; Robb, M. Non-adiabatic dynamics: A comparison of surface hopping direct dynamics with quantum wavepacket calculations. *J. Phys. Chem. A* **2003**, *107*, 621–631.

(68) Cattarius, C.; Worth, G.; Meyer, H.-D.; Cederbaum, L. All mode dynamics at the conical intersection of an octa-atomic molecule: Multi-configuration time-dependent Hartree (MCTDH) investigation on the butatriene cation. *J. Chem. Phys.* **2001**, *115*, 2088–2100.

(69) Worth, G. A.; Robb, M. A.; Burghardt, I. Non-adiabatic Direct Dynamics using Variational Gaussian Wavepackets: The $\tilde{X}/\tilde{A}$ Manifold of the Butatriene Cation. *Faraday Discuss.* **2004**, *127*, 307–323.

(70) Raab, A.; Worth, G.; Meyer, H.-D.; Cederbaum, L. Molecular dynamics of pyrazine after excitation to the S2 electronic state using a realistic 24-mode model hamiltonian. *J. Chem. Phys.* **1999**, *110*, 936–946.

(71) Yamazaki, I.; Murao, T.; Yamanaka, T.; Yoshihara, K. Intramaolecular Electronic Relaxation and Phtoisomerisation Processes in the Isolated Azabenzene Molecules Pyridine, Pyrazine and Pyrimidine. *Faraday Discuss. Chem. Soc.* **1983**, *75*, 395–405.

(72) Worth, G.; Meyer, H.-D.; Cederbaum, L. The effect of a model environment on the S2 absorption spectrum of pyrazine: A wavepacket study treating all 24 vibrational modes. *J. Chem. Phys.* **1996**, *105*, 4412–4426.

(73) Worth, G.; Meyer, H.-D.; Cederbaum, L. Relaxation of a system with a conical intersection coupled to a bath: A Benchmark 24-dimensional wave packet study treating the environment explicitly. *J. Chem. Phys.* **1998**, *109*, 3518–3529.